Time-Dependent Density Matrix Renormalization Group Algorithms for Nearly Exact Absorption and Fluorescence Spectra of Molecular Aggregates at Both Zero and Finite Temperature

Jiajun Ren,[†] Zhigang Shuai,[*,†] and Garnet Kin-Lic Chan[*,‡]

[†]MOE Key Laboratory of Organic OptoElectronics and Molecular Engineering, Department of Chemistry, Tsinghua University, Beijing 100084, People's Republic of China

[‡]Division of Chemistry and Chemical Engineering, California Institute of Technology, Pasadena, California 91125, United States

S *Supporting Information*

ABSTRACT: We implement and apply time-dependent density matrix renormalization group (TD-DMRG) algorithms at zero and finite temperature to compute the linear absorption and fluorescence spectra of molecular aggregates. Our implementation is within a matrix product state/operator framework with an explicit treatment of the excitonic and vibrational degrees of freedom, and it uses the locality of the Hamiltonian in the zero-exciton space to improve the efficiency and accuracy of the calculations. We demonstrate the power of the method by calculations on several molecular aggregate models, comparing our results against those from multilayer multiconfiguration time-dependent Hartree and n-particle approximations. We find that TD-DMRG provides an accurate and efficient route to calculate the spectrum of molecular aggregates.
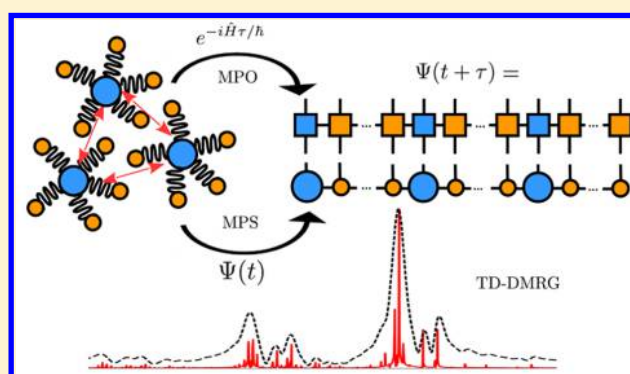
1. INTRODUCTION

The effects of aggregation on the optical and transport properties of molecular aggregates and polymers, such as aggregation induced emission (AIE) in the siloles[1] and ultrafast energy transfer in the photosynthetic light harvesting complexes (LHC),[2] have attracted tremendous attention in the past decades. Understanding the change in the linear spectrum moving from a single molecule to an aggregate is usually the first step to understand the effects of aggregation. Theoretically, the quantitative calculation of the spectrum of molecular aggregates is challenging, as it is a problem of coupled many-particle quantum dynamics, including both excitonic coupling and exciton-vibrational (phonon) coupling.[3] Though perturbative methods are very successful in treating the two limiting coupling regimes[4,5]—the weak excitonic coupling regime and the weak exciton-vibrational coupling regime—many interesting systems, such as the LHC, lie in the intermediate coupling regime and remain challenging to model accurately, motivating the development of a wide variety of approximate modeling methods.[6−17]

Current numerically exact approaches for the intermediate coupling regime work within one of two representations. The first representation is most closely associated with the theory of open quantum system dynamics and dissipative dynamics. Here the whole problem is divided into a system (usually containing the electronic degrees of freedom) and an environment (usually containing the vibrational degrees of freedom). Then, an effective equation of motion for the system part only is derived by eliminating the environmental degrees of freedom, assuming a linear system-environment coupling, and with the environment typically approximated as an infinite harmonic bath described by a continuous spectral density. Some representative numerically exact methods using this representation include the hierarchical equation of motion method (HEOM),[6,7] stochastic Schrödinger equation (SSE),[8,9] hybrids of HEOM and SSE,[10,11] and the quasi-adiabatic propagator path-integral (QUAPI) method.[12] In the second representation, the whole problem is treated explicitly as a closed finite-dimensional system, with discrete vibrational degrees of freedom. Some numerically exact methods commonly employed for such problems include exact diagonalization (ED) and the multiconfiguration time-dependent Hartree (MCTDH) method.[17]

The density matrix renormalization group (DMRG) methods we use in this work are formulated within the second representation, and thus, the most relevant methods to compare against are ED and MCTDH. Full ED, whether applied to the zero-temperature linear spectrum[18] or within the more recent finite-temperature Lanczos formulation,[19,20] is limited to very small systems, as the dimension of the Hilbert space increases exponentially with system size. To overcome

the exponential wall in full ED, systematically improvable approximations can be introduced to reduce the cost, akin to the configuration interaction hierarchy in quantum chemistry.[21,22] One popular example is the so-called "n-particle approximation",[13–16] in which only the electronically excited molecule and at most n−1 nearest ground state molecules are allowed to be simultaneously vibrationally excited. The motivation for this restricted Hilbert space is that a local exciton should only disturb phonon modes nearby, creating an "exciton polaron".[23] Note that the n-particle approximation is also used outside of the ED context; for example, it has recently been used in HEOM to improve efficiency.[24] Though the n-particle approximation method has been applied to explain many features of the spectra of conjugated polymers and molecular aggregates,[23,25] the lowest level two-particle approximation is still too expensive to treat intermediate-sized aggregates with multiple phonon modes, such as multiple molecules with more than 10 modes per molecule, the latter being essential to obtain fine structure in the spectrum.[15] MCTDH is an alternative numerically exact method, based on a low rank tensor representation of the time-dependent wave function. Its generalization—multilayer MCTDH (ML-MCTDH)—has become a popular approach to numerically converge toward the exact quantum dynamics of systems with dozens or even hundreds of quantum degrees of freedom.[26,27] Two algorithms have previously been described to include finite-temperature effects within MCTDH. The first is based on statistical sampling of wave functions from an initial thermal ensemble.[28,29] This approach is numerically efficient in cases when convergence can be reached without too many samples, for example, at low temperatures. However, the scale of temperature is defined relative to the frequencies in the problem; thus, in systems with low frequency modes, where high quanta states would be populated even at room temperature, such an algorithm is not very efficient. The second directly propagates the density matrix of the mixed state by Liouville's equation and is called ρ-MCTDH. It was first explored by Raab et al. in 1999[30,31] and is based on the finite-temperature time-dependent variational principle (TDVP). Unlike the first approach, ρ-MCTDH does not introduce statistical error. However, to our knowledge, the algorithm has not been widely used. One drawback is that propagating the density matrix is more expensive than propagating the wave function. Another drawback is that, unlike at zero temperature, the finite-temperature TDVP that was used violates the conservation of the total energy and density matrix trace.[32]

In the current work, we consider an alternative numerical approach to obtain near-exact zero-temperature and finite-temperature spectra, via the time-dependent density matrix renormalization group (TD-DMRG). Much like ML-MCTDH, the DMRG is based on a low-rank tensor representation of the wave function. It was originally proposed by White to treat one-dimensional strongly correlated systems, where it has become the method of choice to compute low-lying eigenstates.[33,34] The DMRG was subsequently extended to frequency-dependent dynamic properties, via the Lanczos DMRG,[35] correction-vector DMRG,[36] and the dynamical DMRG methods.[37] These closely related algorithms all provide dynamic properties at zero temperature in the frequency domain. DMRG algorithms have also been formulated at finite temperature. The earliest attempts used renormalization of the transfer matrix (TMRG),[38–40] but more systematic finite-

temperature formulations emerged out of time-dependent density matrix renormalization group (TD-DMRG) algorithms,[41–50] which also provide a route to real-time zero-temperature dynamical properties. In particular, the thermal state can be obtained by imaginary time-propagation (either within a purified state formalism or via propagation of operators) and subsequent propagation along the real-time axis then allows for the computation of finite-temperature dynamical quantities.[51–54]

DMRG methods have been applied to a wide variety of problems in chemical physics. Semiempirical DMRG and ab initio DMRG methods have been developed in the last two decades for molecular quantum chemistry problems[55,56] including for the calculation of dynamical properties.[50,57] DMRG methods have also been applied to electron−phonon problems, including the spin-Peierls model,[58] and to the single-mode Holstein model.[59–61] Finally, TD-DMRG methods have been recently applied to open quantum system dynamics, both in the context of impurity problems,[62–65] as well as traditional system-bath models.[66–70]

In this work, we develop TD-DMRG algorithms for zero- and finite-temperature dynamic properties of electron−phonon-coupled systems, as applied to the linear absorption and fluorescence spectra of electron−phonon-coupled molecular aggregates. As a nonperturbative method, we will show that these algorithms allow us to compute accurate spectra across any range of coupling strengths. Furthermore, we will demonstrate that the high efficiency of the TD-DMRG algorithm allows us to calculate the spectrum for a system as large as an 18 monomer distyryl benzene (DSB) aggregate, including the fine structure from the phonon modes.

The remaining sections of this paper are arranged as follows. In Section 2, we first define the Hamiltonian of the exciton model used in this work. Next, we describe the zero- and finite-temperature TD-DMRG methods used to calculate the absorption and fluorescence spectra and provide some computational details. In Section 3, the absorption and fluorescence spectra of both model and real systems are calculated and compared to that from ML-MCTDH, the n-particle approximation, and experimental spectra. Finally, we present our conclusions in Section 4.

2. THEORY

2.1. Model Hamiltonian. To map the spectral problem for a set of molecular aggregates to a practically solvable model, we first make several (reasonable) approximations:

(i) The electronic excited states of a molecular aggregate are a linear combination of the local excited states of a single molecule.

(ii) The motion of the nuclei can be described as a collection of independent harmonic vibrations.

(iii) Only intramolecular vibrations are considered to be linearly coupled to the local electronic state, where the frequency ω of each vibration is the same for both the ground and excited states.

The combination of the second and third approximations is usually referred to as the "displaced harmonic oscillator" approximation. Within these approximations, we can map the Hamiltonian of a molecular aggregate to a multimode Holstein Hamiltonian, sometimes called the "Frenkel" or "Frenkel−Holstein" Hamiltonian. In addition, we can add additional processes to the Hamiltonian, relaxing the above three

assumptions, such as intermolecular charge-transfer states,[16,71,72] anharmonic vibrational effects,[73] and intermolecular electron−phonon interactions (Peierls terms). For simplicity, however, we will only consider the Holstein Hamiltonian in this work.

Choosing harmonic oscillator wave functions within the ground state potential energy surface as the vibrational basis, the Hamiltonian can be formulated in second quantization

$$\hat{H} = \sum_i \varepsilon_i a_i^\dagger a_i + \sum_{ij} J_{ij} a_i^\dagger a_j$$
$$+ \sum_{in} \omega_{in} b_{in}^\dagger b_{in} + \sum_{in} \omega_{in} g_{in} a_i^\dagger a_i (b_{in}^\dagger + b_{in})$$

$$(1)$$

ε_i is the local excited state energy of molecule i; J_{ij} is the excitonic coupling between molecule i and j; ω_{in} and g_{in} are, respectively, the harmonic frequency and electron-vibrational coupling parameter of normal mode n of molecule i. Another alternative parameter frequently used to represent the strength of electron-vibrational coupling is Huang−Rhys factor S, where $S = g^2$. All the parameters can be obtained from ab initio quantum chemistry calculations of monomers and dimers, or fitted to experimental data. The vibrational modes in eq 1 are considered to be discrete, as is appropriate for single molecules or small aggregates. In contrast, in the condensed phase, one often describes the behavior of the macroscopic bath in terms of a continuous spectral density function

$$J_i(\omega) = \pi \sum_n (g_{in}\omega_{in})^2 \delta(\omega - \omega_{in})$$

$$(2)$$

To use the methods in this work with such a formulation, one has to first discretize the spectral density. There are many such discretization algorithms that have been explored in studies of quantum impurity problems and to describe open-system quantum dynamics.[64,74−77] We will only consider the discrete modes associated with molecular aggregates here, and thus, we will not dive further into the details of discretizing a continuous bath.

2.2. MPS, MPO, ZT-TD-DMRG, and FT-TD-DMRG. The theory of DMRG and its associated algorithms has been described in detail in many excellent reviews.[78] Here, to be self-contained, we only briefly summarize the most essential parts.

2.2.1. MPS and MPO. DMRG is a wave function theory, where the many-body wave function amplitudes are obtained by multiplying out a chain of local matrices (thus giving rise to the moniker, matrix product state (MPS)),

$$|\Psi\rangle = \sum_{\{\sigma\}} C_{\sigma_1\sigma_2\cdots\sigma_n}|\sigma_1\sigma_2\cdots\sigma_n\rangle$$
$$= \sum_{\{a\},\{\sigma\}} A_{a_1}^{\sigma_1} A_{a_1 a_2}^{\sigma_2} \cdots A_{a_{n-1}}^{\sigma_n} |\sigma_1\sigma_2\cdots\sigma_n\rangle$$

$$(3)$$

a_n is the virtual bond index, whose "bond dimension" controls the accuracy of a DMRG calculation and the amount of entanglement captured by the MPS. σ_n is called the physical bond index, and it indexes the degrees of freedom of a single site. The MPS can be represented graphically as shown in Figure 1a. There is a gauge freedom (redundancy in parametrization) in the MPS which can be fixed by requiring the matrices to the left or right of any given bond to satisfy respectively the left and right orthogonality conditions, $\sum_\sigma \mathbf{A}^{\sigma\dagger}\mathbf{A}^\sigma = \mathbf{I}$, $\sum_\sigma \mathbf{A}^\sigma \mathbf{A}^{\sigma\dagger} = \mathbf{I}$, respectively (see Figure 1b,c).
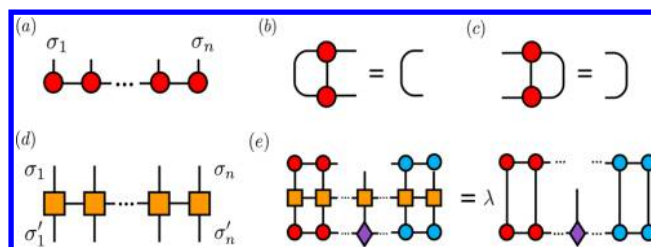
Figure 1. Graphical representation of (a) an MPS for Ψ (b) the left orthogonality condition (c) the right orthogonality condition (d) an MPO for $\hat{O}$ (e) the ground-state eigenvalue equation for $\hat{H}\psi = \lambda\psi$. Each linked bond represents a tensor contraction.

The structure of the MPS wave function is related to that of the ML-MCTDH wave function. In particular, the ML-MCTDH wave function can be thought of as a tree factorization of the wave function amplitudes, also known as a tree tensor network state.[79] Thus, viewed from the ML-MCTDH perspective, the linear chain of matrices in the MPS formally corresponds to a maximally unbalanced tree, although such a tree structure is seldom used in ML-MCTDH. An advantage of the MPS structure over a more general tree is that almost all numerical operations can be implemented as simple matrix operations rather than more general tensor contractions. In practical applications, this can lead to higher efficiency.[80]

In the Holstein model we consider, there are both exciton and vibrational physical degrees of freedom. We associate each exciton and each vibration with its own matrix $\mathbf{A}^\sigma$ where σ indexes the exciton or vibrational state. The exciton site has two states, $|0\rangle$ representing the electronic ground state and $|1\rangle$ representing the electronic excited state. The vibrational site has p states, $|0\rangle$, $|1\rangle$, $\cdots|p-1\rangle$ representing the number of phonons (in principle p is infinite, but at low temperature, we can converge static and dynamic properties with a finite p). In addition, the MPS is not invariant to the order in which the degrees of freedom are treated. We order the exciton and vibration degrees of freedom by molecule, that is $e_1, \nu_{11}, ..., \nu_{1n}, ..., e_i, \nu_{i1}, ..., \nu_{in}, ...(e_i$ is the exciton site of molecule i, ν_{in} is nth mode of molecule i).

When constructing MPS algorithms, it is convenient to consider a related factorization of operators. There, operator matrix elements are obtained by multiplying out a chain of local matrices, giving rise to a matrix product operator (MPO)

$$\hat{O} = \sum_{\{a\},\{\sigma\},\{\sigma'\}} W_{a_1}^{\sigma_1,\sigma'_1} W_{a_1 a_2}^{\sigma_2,\sigma'_2} \cdots W_{a_{n-1}}^{\sigma_n,\sigma'_n} |\sigma_1\sigma_2\cdots\sigma_n\rangle\langle\sigma'_1\sigma'_2\cdots\sigma'_n|$$

$$(4)$$

Similar to the gauge freedom in an MPS, there are many choices of local matrices in the MPO which multiply out to the same total operator $\hat{O}$.[81] One optimal way to construct the MPO of the Holstein Hamiltonian in our work is given in Appendix A.

To approximate a quantum ground state, we optimize the MPS matrices following the variational principle. Rather than optimize all matrices simultaneously, one typically optimizes the matrices one at a time, and this is the basis of the one-site DMRG algorithm. At each optimization step, the sites are partitioned into two blocks, A and B, and an eigenvalue equation is solved in a space spanned by the direct product of the A and B block basis states $|l\rangle_A \otimes |r\rangle_B$, defined by the MPS matrices to the left and right of the partitioning bond,
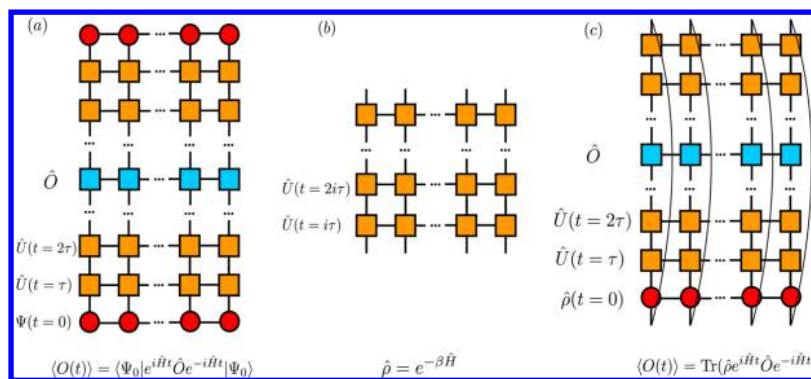
Figure 2. Graphical representation of (a) $\langle \hat{O}(t) \rangle$ at zero temperature (b) the density operator $e^{-\beta \hat{H}}$ (c) $\langle \hat{O}(t) \rangle$ at finite temperature. The long line linking the top and bottom physical bonds represents a trace. Compression is carried out after each application of the unitary propagator in ascending time in (a), (b), and (c).

respectively. If the gauge has been fixed such that sites in block A and block B satisfy left and right orthogonality conditions, then the eigenvalue equation takes the form

$$\sum_{l'r'} H_{lrl'r'}\psi_{l'r'} = E\psi_{lr} \tag{5}$$

The quantities in the matrix eigenvalue equation and the block basis states are most easily visualized graphically (see Figure 1e). The eigenvalue problem in eq 5 can be computed iteratively by the Davidson algorithm via series of tensor contractions with cost $O(2pM^3D + p^2M^2D^2)$ in each iteration, giving a total cost of $O(k_e k_\nu (2pM^3D + p^2M^2D^2))$ for one sweep of optimization steps over all sites. Here, k_e is the number of molecules; k_ν is the number of normal modes of each molecule; p is the number of local degrees of freedom; M is the MPS virtual bond dimension; D is the MPO bond dimension. For the Holstein Hamiltonian, when considering only one-dimensional nearest-neighbor excitonic couplings, $D \sim$ const, otherwise $D \sim k_e$.

An important MPS algorithm is the compression of a large bond dimension MPS to a smaller bond dimension MPS. Compression is necessary because many algebraic operations involving MPS increase the bond dimension, such as acting an MPO on an MPS, or adding together two MPS (both operations are used in the time-dependent algorithms below). The simplest compression algorithm is the singular value decomposion (SVD) compression algorithm. Given the wave function ψ_{lr} in eq 5 on a given bond, we decompose it via SVD as

$$\psi_{lr} \approx \sum_{d=1}^{M} s_d U_{ld} V_{dr}^\dagger \tag{6}$$

where s_d are the singular values which can be truncated to some desired number M. Multiplying the truncated **U** and **V** matrices into the matrices to the left and right of the bond reduces the bond dimension joining the two matrices. The compression can then be repeated for the next bond and iterated through the entire MPS. A closely related compression algorithm is the variational compression algorithm, where a compressed $|\tilde{\psi}\rangle$ with the desired reduced bond dimension is optimized to minimize the L_2 norm $|||\psi\rangle - |\tilde{\psi}\rangle||_2$, leading to a set of least-squares equations to be solved at each site. In this work, we employ the SVD algorithm for our MPS compressions.

2.2.2. ZT-TD-DMRG and FT-TD-DMRG. We now describe the zero-temperature and finite-temperature time-dependent DMRG algorithms. For zero-temperature TD-DMRG (ZT-TD-DMRG), we consider the initial state to be the ground-state MPS obtained via the above DMRG algorithm within a given exciton number sector (we track the exciton number as a good quantum number in the MPS sweep), that is, the zero- (one-) exciton space for absorption(fluorescence). We then need to propagate the state under the time-independent Hamiltonian propagator $e^{-i\hat{H}t}$. In the language of MPS and MPO, the task is to approximate the propagator as an MPO and the subsequent time-evolved state as an MPS in a computationally efficient manner. There are several choices for how to do this, ranging from Suzuki–Trotter decompositions that are most natural for Hamiltonians with short-range interactions,[43] to time-step targeting and other techniques[46,57,82] designed for Hamiltonians with long-range interactions.

We use the classical fourth-order Runge–Kutta (RK4) algorithm together with an MPO representation of the full Hamiltonian to carry out a single time-step propagation

$$|k_1\rangle = -i\hat{H}(t)|\Psi(t)\rangle$$

$$|k_2\rangle = -i\hat{H}(t + \tau/2)\left(|\Psi(t)\rangle + \frac{1}{2}\tau|k_1\rangle\right)$$

$$|k_3\rangle = -i\hat{H}(t + \tau/2)\left(|\Psi(t)\rangle + \frac{1}{2}\tau|k_2\rangle\right)$$

$$|k_4\rangle = -i\hat{H}(t + \tau)(|\Psi(t)\rangle + \tau|k_3\rangle)$$

$$|\Psi(t + \tau)\rangle = |\Psi(t)\rangle + \frac{1}{6}\tau(|k_1\rangle + 2|k_2\rangle + 2|k_3\rangle + |k_4\rangle) \tag{7}$$

Here, τ is the time step, $\hat{H}(t)$ is an MPO and each wave function $|k_i\rangle$ is an MPS. The stable region for the time step τ requires the RK4 propagator to have modulus <1. As described in the Supporting Information (SI) (section 1), for real-time propagation, $\tau \cdot e < 2.828$, and for imaginary time propagation, $\tau \cdot e < 2.785$, where e is the absolute maximal eigenvalue of $\hat{H}$. In practice, to simulate with as large a time-step as possible, one usually defines $\hat{H}(t)$ with the lowest state energy subtracted. Note that for time independent Hamiltonians, the RK4 method reverts back to eq 8, which is nothing but a fourth-order Taylor expansion of $e^{-i\hat{H}\tau}$ around time 0.

$$e^{-iH\tau} \approx 1 + (-iH\tau) + \frac{(-iH\tau)^2}{2!} + \frac{(-iH\tau)^3}{3!} + \frac{(-iH\tau)^4}{4!} \tag{8}$$

During each time step propagation, $\hat{H} \cdot \Psi$ is carried out for four times. At each time, the virtual bond dimension a_n of MPS is enlarged by a factor of D and thus needs to be compressed. We carry out compression back to the desired bond dimension M using the SVD algorithm described previously. Overall, the graphical representation of the expectation value $\langle O(t)\rangle$ at zero temperature computed using ZT-TD-DMRG is shown in Figure 2a.

For finite-temperature TD-DMRG (FT-TD-DMRG), we must first represent the initial thermal state in matrix product form. The most common method to achieve this is via the thermo field dynamics approach (or called "purification" or "ancilla" approach).[51−53,83,84] The basic idea is to represent a mixed state density operator as a partial trace of a pure state density operator in an enlarged space, namely, the physical space $P \otimes$ an auxiliary space Q. The simplest choice is to choose Q identical to the physical space P

$$\hat{\rho} = \sum_i s_i |i\rangle\langle i| = \mathrm{Tr}_Q |\Psi\rangle\langle\Psi|$$

$$|\Psi\rangle = \sum_i s_i^{1/2} |i\rangle_P |i\rangle_Q \tag{9}$$

Then, the thermal equilibrium density operator can be expressed as

$$\hat{\rho}_{eq} = \frac{e^{-\beta\hat{H}}}{Z(\beta)} = \frac{\mathrm{Tr}_Q |\Psi_\beta\rangle\langle\Psi_\beta|}{\mathrm{Tr}_{PQ} |\Psi_\beta\rangle\langle\Psi_\beta|}$$

$$|\Psi_\beta\rangle = e^{-\beta\hat{H}/2}|\Psi_\infty\rangle, \ |\Psi_\infty\rangle = \sum_i |i\rangle_P |i\rangle_Q \tag{10}$$

where $\hat{H} = \hat{H}_P \otimes \hat{I}_Q$ and $|\Psi_\infty\rangle$ is an unnormalized product of maximally entangled states between each physical site and a corresponding auxiliary site. To obtain $|\Psi_\beta\rangle$, imaginary time propagation is carried out on the initial state $|\Psi_\infty\rangle$, and once temperature β is reached, real-time propagation is carried out on $|\Psi_\beta\rangle$. Since all operations are on pure states, the finite-temperature algorithm can be implemented using exactly the same code as the zero-temperature algorithm, the only difference being that the total size of the system (i.e., the number of sites) is increased by a factor of 2. However, in terms of MPO's, we can equivalently understand the finite-temperature method as a direct propagation of the density matrix, eliminating the need for ancillas[54] (see Figures 2b,c). In this case, the initial infinite-temperature density matrix $|\Psi_\infty\rangle$ is simply an identity operator in the Hilbert space and is an MPO with bond dimension 1. Then the thermal equilibrium density operator can be expressed as

$$e^{-\beta\hat{H}} = e^{-\beta\hat{H}/2}\hat{I}e^{-\beta\hat{H}/2} \tag{11}$$

To carry out the MPO time propagation, MPO compression is carried out at each step by interpreting an MPO as an MPS where the two physical indices on each site are viewed as the physical index of an MPS in an enlarged space, making the MPO compression identical to the MPS compression in the ancilla picture. Note that the initial high-temperature density matrix $\hat{I}$ can in principle be replaced by any unitary operator $\hat{U}$, since

$$e^{-\beta\hat{H}} = e^{-\beta\hat{H}/2}\hat{U}\hat{U}^\dagger e^{-\beta\hat{H}/2} \tag{12}$$

and this degree of freedom has recently been used to reduce the entanglement growth and thus cost of time propagation.[85] In our FT-TD-DMRG implementation, we use the MPO propagation formulation starting from an initial identity operator.

The most time-consuming part in the TD-DMRG algorithm is the SVD compression. The computational scaling of the SVD compression is roughly $O(Nk_ek_\nu pM^3D^3)$ for ZT-TD-DMRG and $O(Nk_ek_\nu p^2M^3D^3)$ for FT-TD-DMRG (N is the number of propagation steps). We see that the only difference in formal scaling arises from the increase in physical bond dimension going from ZT to FT (p to p^2). However, the bond dimension M necessary for a given accuracy will be different in the finite-temperature and zero-temperature formulations. To see this, consider the zero-temperature limit or a pure state, where the density matrix in the FT-TD-DMRG formulation can be trivially expressed as

$$\rho = |\Psi\rangle\langle\Psi|$$

$$= \sum_{\{a,a'\},\{\sigma,\sigma'\}} (A_{a_1}^{\sigma_1} A_{a'_1}^{\sigma'_1})(A_{a_1 a_2}^{\sigma_2} A_{a'_1 a'_2}^{\sigma'_2})\cdots(A_{a_{n-1}}^{\sigma_n} A_{a'_{n-1}}^{\sigma'_n})$$

$$|\sigma_1\sigma_2\cdots\sigma_n\rangle\langle\sigma'_1\sigma'_2\cdots\sigma'_n|$$

$$= \sum_{\{b\},\{\sigma,\sigma'\}} B_{b_1}^{\sigma_1,\sigma'_1} B_{b_1 b_2}^{\sigma_2,\sigma'_2}\cdots B_{b_{n-1}}^{\sigma_n,\sigma'_n}|\sigma_1\sigma_2\cdots\sigma_n\rangle\langle\sigma'_1\sigma'_2\cdots\sigma'_n| \tag{13}$$

where $\dim(b_i) = \dim(a_i)\cdot\dim(a'_i)$. This shows that the bond dimension for a given accuracy in the FT-TD-DMRG at low temperature is the square of that in the ZT-TD-DMRG formulation.

With ZT-TD-DMRG and FT-TD-DMRG, the absorption and fluorescence spectra can be calculated by taking the Fourier transform of the dipole−dipole time correlation function.

$$\sigma_{\mathrm{abs(emi)}}(\omega) \propto \frac{1}{2\pi}\int_{-\infty}^{+\infty} dt e^{i\omega t} C(t) \tag{14}$$

$$C(t) = \langle\hat{\mu}(t)\hat{\mu}(0)\rangle_{g(e)} \tag{15}$$

The subscript $g(e)$ represents the zero-(one-) exciton ground (excited) state space. The bracket denotes the lowest energy state expectation value at zero temperature and the thermal equilibrium average at finite temperature. The frequency dependence of the prefactor is, respectively, ω and ω^3 for the absorption and emission cross section. To apply a Gaussian broadening in the frequency domain (convolving the original spectrum with a Gaussian function), we multiply the dipole−dipole correlation function in the time domain with a Gaussian function (pointwise) before the Fourier transform

$$C'(t) = C(t)e^{-(t/t_{\mathrm{Gaussian}})^2} \tag{16}$$

where the connection between broadening in the time domain and in the frequency domain is provided by the Convolution Theorem.

2.3. Computational Optimizations. We now consider some techniques to improve the efficiency and accuracy of time propagation for the specific case of the Holstein Hamiltonian. When calculating the linear spectrum, the excited state is in the one-exciton space, while the ground state is in the zero-exciton space. In the zero-exciton space, the

Hamiltonian in eq 1 becomes trivial—only the vibrational energy terms survive. These terms are local and commute with each other

$$\hat{H}_g = \sum_{in} \omega_{in} b_{in}^{\dagger} b_{in} \tag{17}$$

Thus, unlike the propagator in the one-exciton space that is approximated by the RK method, the propagator in the zero-exciton space can be exactly represented as an MPO with bond dimension 1

$$e^{-i\hat{H}_g t} = e^{-i\hat{H}_{g1} t} e^{-i\hat{H}_{g2} t} \cdots e^{-i\hat{H}_{gn} t} \tag{18}$$

Therefore, time propagation in the zero-exciton space is exact and MPS compression is not required.

For example, the dipole−dipole time correlation function in eq 14 for the zero-temperature fluorescence spectrum is

$$C(t) = e^{iE_e t} \langle \Psi_e(0)|\hat{\mu} e^{-i\hat{H}_g t} \hat{\mu}|\Psi_e(0)\rangle \tag{19}$$

Here, $|\Psi_e(0)\rangle$ and E_e are the wave function and energy of the lowest excited state in the one-exciton space. Since the single lowest excited state can be accurately obtained with the standard DMRG algorithm with a modest virtual bond dimension, and the subsequent time propagation under $\hat{H}_g$ does not increase the bond dimension, the zero-temperature fluorescence spectrum can be calculated without the cost of a full TD-DMRG calculation. Note that the same technique can be applied to other observables where propagation is restricted to the zero-exciton space.

Another potential optimization in TD-DMRG is to carry out a basis transformation to minimize the growth of entanglement. In the Holstein Hamiltonian in eq 1, every exciton site is coupled to a set of vibration sites, leading to a "star-like" topology for the exciton−phonon interactions. An alternative topology is a "chain" topology that can be obtained via a unitary rotation of the vibrational basis.[64,74] We have compared the two representations in our calculations and found that the "star" representation generally introduces less entanglement (see SI section 3). Thus, we use the "star" representation in our calculations.
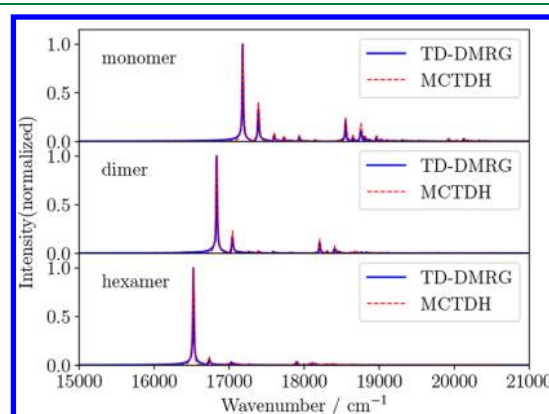
3. RESULTS

3.1. Linear Spectrum of PBI J-Type Aggregates. From a purely excitonic coupling perspective, two typical aggregation types have been defined by Kasha.[86] One is the J-type aggregate, where the sign of the excitonic coupling is negative (assuming the transition dipole moments all point in the same direction), as is the case for molecules packed in a "head-to-tail" orientation. In the lowest (highest) excitonic band, the dipole moments of the molecules interfere constructively (destructively), so the absorption and fluorescence are enhanced and red-shifted. Another is the H-type aggregate, in which the molecules are stacked in a "side-by-side" orientation, resulting in a positive excitonic coupling. In contrast to the J-type aggregates, the absorption is blue-shifted, and the fluorescence is suppressed.

Perylene bisimide dyes (PBI) are prototypical building blocks for H- and J-type molecular aggregates, and they are potential candidates for an artificial light-harvesting system.[87] The optical properties have been investigated both experimentally and theoretically. Among the reported theoretical calculations of the linear spectrum of J-type PBI, the ML-MCTDH calculations by Kühn et al. are probably the most

accurate. The first set of ML-MCTDH calculations were presented in ref 88 with the largest system treated being a linear hexamer, including up to 5 vibrational modes per molecule. Subsequently, improved calculations including 10 modes per molecule were reported.[3] The ML-MCTDH calculations were all at zero temperature, and the finite-temperature spectrum was not computed.

To verify the correctness of our TD-DMRG implementation, we first calculated the zero-temperature linear absorption of a PBI chain, and we compared our results to those from ML-MCTDH using the parameters of the ML-MCTDH calculations with 10 phonon modes.[3] We used a total evolution time τ of 20 a.u., $N = 20000$ time steps, and an SVD cutoff of 10^{-3}. The maximal virtual bond dimension is 42. We applied a Gaussian broadening $C(t)e^{-(t/t_{Gaussian})^2}$ in the time domain with $t_{Gaussian} = 2000$ fs.

In Figure 3, we show the zero-temperature absorption spectrum computed from ZT-TD-DMRG. The spectrum is

Figure 3. Calculated zero-temperature linear absorption spectra of the PBI monomer, dimer, and hexamer from ZT-TD-DMRG. Each molecule includes 10 normal modes. The ML-MCTDH results are from ref 3.

essentially identical to that obtained by ML-MCTDH. Two main vibronic structures can be identified. One is due to a high-frequency mode $\omega = 1371$ cm^{-1}, $S = 0.208$ and the other is due to two modes with similar frequencies and Huang−Rhys factors $\omega = 206, 211$ cm^{-1}, $S = 0.197, 0.215$. The remaining modes cannot be clearly assigned because of their small Huang−Rhys factors (<0.1).

Using our FT-TD-DMRG implementation, we can further extend our calculations to obtain the finite-temperature absorption and fluorescence spectra. We calculated the spectrum of the PBI dimer at 298 K, which can be compared against the reported experimental spectrum[89] (see Figure 4). We see that the spectra agree well but the 0−0 transition peak is slightly shifted from the experimental position. The fine structure of the room-temperature spectrum is also well reproduced, except for the absorption peak near 450 nm. This peak originates from the second local electronic excited state,[88] which is not contained in our model Hamiltonian. Unfortunately, there are no finite-temperature MCTDH results reported for this system for comparison.

In conjunction, our calculations on the PBI systems show that TD-DMRG is a high level quantum dynamics method and a practical alternative to ML-MCTDH, achieving good accuracy at finite as well as at zero temperatures.
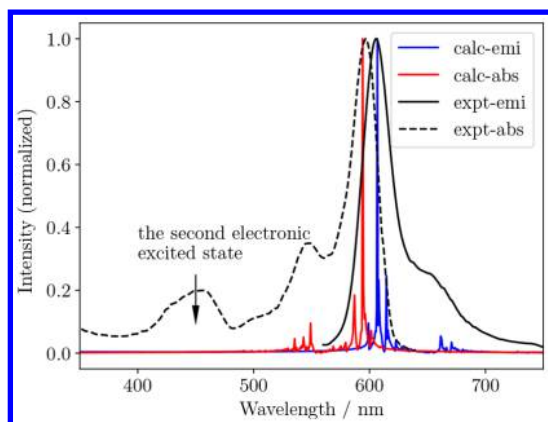
Figure 4. Calculated absorption and fluorescence spectra of PBI dimer at 298 K from FT-TD-DMRG. The SVD cutoff is 10^{-3}, total simulation time $\tau = 20$ a.u., and total number of time-steps $N = 5000$. The maximal virtual bond dimension is 120. No broadening is applied. The experimental spectrum from ref 89 is also plotted.
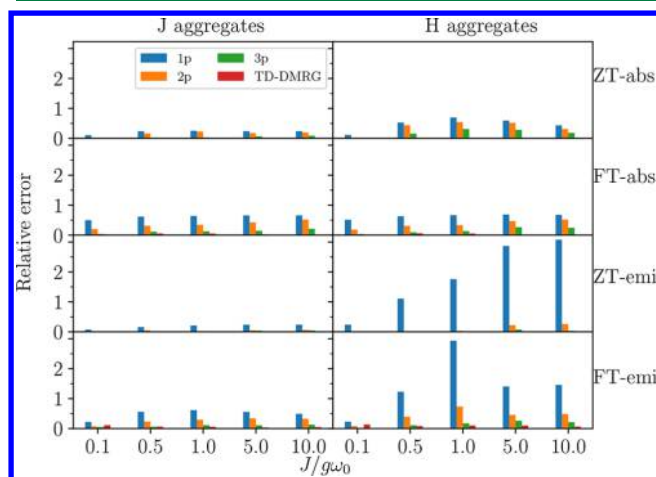
3.2. TD-DMRG vs the n-Particle Approximation.

The n-particle approximation is a popular method to calculate the linear spectrum of molecular aggregates. However, for small n, it is only accurate in the weak excitonic coupling regime. We now compare TD-DMRG with 1-, 2-, 3- particle approximations in a model chain system, composed of 4 identical molecules, with nearest-neighbor excitonic coupling and periodic boundary conditions. We choose each molecule to have a single vibration mode and for each mode to have up to 8 phonons. Full ED can be carried out as an exact reference in this system. We use the n-particle approximation with respect to the Hamiltonian and basis in eq 1, without first carrying out a Lang–Firsov transformation as is done in some other works.[13,14,23,90] Note that the Lang–Firsov transformation for an infinite phonon space is unitary, but for a truncated phonon space, it is not. Thus, the results with or without Lang–Firsov transformation will be a little bit different, but this difference will be negligible at low temperatures.

We calculated the zero- and finite-temperature absorption and fluorescence spectra for both J- and H- type aggregates. We set the Huang–Rhys factor to 1.0, the temperature to be $k_b T = \hbar\omega_0$ and varied the excitonic coupling to the exciton–phonon coupling ratio $J/g\omega_0$. The SVD cutoff in ZT-TD-DMRG was set to 10^{-4} and that of FT-TD-DMRG to 10^{-3}. For a direct comparison with TD-DMRG, the full ED and n-particle approximation spectra were also obtained by time-propagation. All propagations were carried out with a time step $\tau = \frac{0.032}{\omega_0}$ and a total number of steps $N = 20000$. A small Gaussian broadening was applied to increase the smoothness of the spectrum, $t_{Gaussian} = \frac{131}{\omega_0}$. To compare the various spectra, we use the relative error of the spectrum compared to the exact result from full ED

$$\text{relative error}_{method} = \frac{\sum_{i=1}^{N} |\sigma_{method}(\omega_i) - \sigma_{exact}(\omega_i)| d\omega}{\sum_{i=1}^{N} \sigma_{exact}(\omega_i) d\omega}$$

(20)

where ω_i is a discrete point in the frequency domain and $\sigma(\omega_i)$ is the strength at frequency ω_i. The relative error of the different methods is shown in Figure 5. Note that in the n-particle approximation, since even the 0–0 energy gaps

changes with n, we shift all the spectra by subtracting the 0–0 energy gap.

Figure 5. Relative error of the absorption and emission spectra at both zero and finite temperature from four different methods, TD-DMRG (red), 1-(blue), 2-(orange), 3-(green) particle approximation methods. The excitonic/exciton–phonon coupling ratio is 0.1, 0.5, 1.0, 5.0, and 10.0.

Our calculations show that the accuracy of TD-DMRG greatly surpasses that of n-particle approximation methods in all cases. The error of FT-TD-DMRG is a little larger than that of ZT-TD-DMRG calculation, probably due to the larger cutoff threshold in the SVD. In the coupling regime where J and $g\omega_0$ are comparable, also known as the strongly correlated regime, the virtual bond dimension of the MPS increases much more rapidly than in the two limiting coupling regimes. This rapid increase in bond dimension coincides with the breakdown of perturbation theory in this regime.

For the n-particle approximation, we find a wide variation in the accuracy depending on the simulation regime. In particular, we find that (i) In the weak excitonic coupling regime $J/g\omega_0 = 0.1$, the n-particle approximations perform well. However, when $J/g\omega_0$ is larger than 0.5, the error is large. There is no simple trend in the error as a function of $J/g\omega_0$. (ii) The finite-temperature spectrum is worse than the zero-temperature spectrum. When the temperature is increased, in addition to the single electronically excited molecule itself, additional molecules in the ground state become vibrationally excited, which are not included in the n-particle approximation. Therefore, the n-particle approximation is only good for targeting the lowest energy states. When high energy states contribute to the spectrum, the results worsen. (iii) The 1-particle approximation results for the emission of H-type aggregates are not reliable, as they overestimate the 0–1 emission (see Figure 6). Taking the dimer as an example, the vector $|e_1\nu_1,e_2\nu_2\rangle$ denotes an occupation representation of the dimer basis. ($|e_i\rangle$ represents an exciton, $|\nu_i\rangle$ represents a vibrational mode). In the 1-particle approximation space, only the $|10,00\rangle$, $|00,10\rangle$, $|11,00\rangle$, $|00,11\rangle$ states are considered. The last two basis states contribute to the 0–1 emission strength. The $|01,10\rangle$, $|10,01\rangle$ states which are included in the 2-particle approximation, do not appear. However, these two neglected basis states are important because they directly electronically couple to $|11,00\rangle$, $|00,11\rangle$. In H-type aggregates, the wave function amplitudes for $|11,00\rangle$ and $|01,10\rangle$ (or $|10,01\rangle$ and $|$
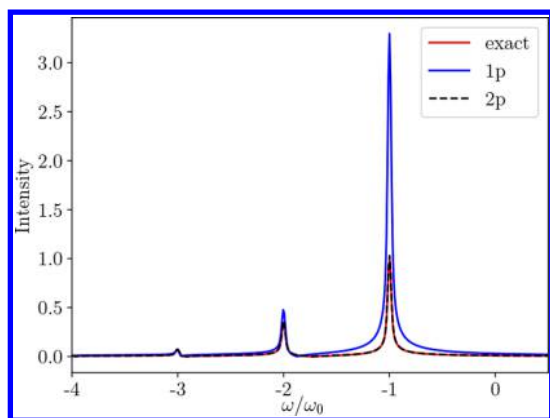
Figure 6. Zero-temperature emission of a H-type chain model for $J/g\omega_0 = 1$. The spectrum is scaled by a factor which normalizes the exact spectrum. The 0−0 position is shifted to the origin. The results of three methods are shown, exact(red), 1-particle(blue), 2-particle-(black dotted) approximation.

$00,11\rangle)$ are opposite in sign, so they contribute to decreasing the 0−1 strength from that when only the $|11,00\rangle$, $|00,11\rangle$ states are in the Hilbert space, as in the 1-particle approximation. This explains why the 2-particle approximation improves the 0−1 emission dramatically. We thus recommend that the 2-particle approximation is the lowest level n-particle approximation to use when calculating the fluorescence spectrum of H-type aggregates.

3.3. TD-DMRG: Sources of Error.
To better understand the errors in the TD-DMRG propagation, we can separate the two sources of error that arise, namely, from the DMRG compression and from the RK evolution. To study the DMRG error by itself (at zero temperature), at each time step $t \to t + \tau$, we expand the wave function $\Psi_{DMRG}(t)$ in the DMRG representation into a full configuration interaction (FCI) representation $\Psi_{FCI}(t)$, which is then propagated by an exact propagator (calculated by ED) to $\Psi_{FCI}(t + \tau)$, before being compressed into the DMRG representation $\Psi_{DMRG}(t + \tau)$ by SVD under a specified compression criterion. To analyze the RK error by itself, all steps are performed within the FCI representation.

In Figure 7a, we plot the error of the TD-DMRG wave function $(\Psi(t) = e^{-i\hat{H}t}\hat{\mu}\Psi_g(0))$ due to the DMRG compression alone for different SVD cutoffs or bond dimensions M, for the same model J-type aggregates with $J/g\omega_0 = 1.0$ (the challenging intermediate coupling regime). The time step τ and the total number of propagation steps N are the same as in the previous section. For fixed SVD cutoff, the wave function error initially grows smoothly, with a polynomial growth as a function of propagation time. Interestingly, for fixed bond dimension, the error versus time shows a "three-stage" structure. The error is initially quite small and then grows very quickly, finally reaching a regime where it increases smoothly with time similarly to the case of fixed SVD cutoff. In Figure 7b, the bond dimension versus time is also plotted. When the SVD cutoff is fixed, the maximal bond dimension grows up to a certain value instead of growing indefinitely, and this value increases as the SVD cutoff is tightened. Thus, comparing panels a and b of Figure 7, the "three-stage" structure of the error for fixed bond dimension M arises because (i) in the first stage, M is larger than the required M_{req} for exact evolution, giving a very small total error (controlled by the round-off error); (ii) in the second "rapid growth" stage,
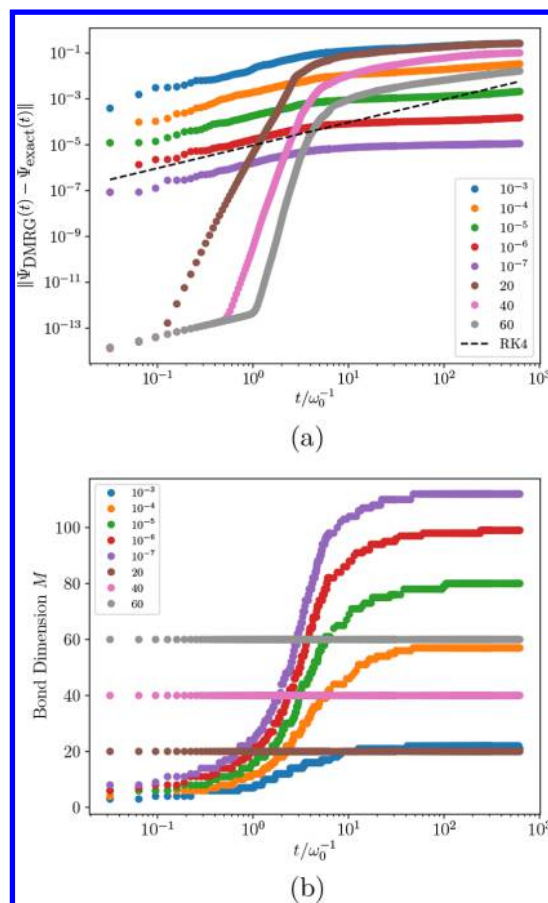
**Figure 7.** (a) Error $\|\Psi_{DMRG}(t) - \Psi_{exact}(t)\|$ and (b) the maximal bond dimension M of the DMRG wave function as a function of time under different compression criteria (fixed SVD cutoffs: 10^{-3}, 10^{-4}, 10^{-5}, 10^{-6}, 10^{-7} and fixed bond dimensions: 20, 40 and 60). The error due to the RK4 integration is also plotted (black dashed line).

the M_{req} for maintaining a given accuracy increases very quickly past the fixed M, and thus, the error increases rapidly; (iii) finally in the third stage, the growth rate of M_{req} for a certain accuracy slows down, and thus, the error grows smoothly again.

The formal relation between the global error due to the RK4 integration and time (total time t and time step τ) is well-known and is $O(t\tau^4)$. In our problem, the error due to RK4 integration is shown in Figure S2, which is consistent with the above relation.

Comparing the RK4 integration error and the DMRG compression error within the time window calculated, the error due to RK4 is smaller than that due to DMRG compression, for the SVD cutoffs of 10^{-3} and 10^{-4} (see Figure 7a, black dashed line). In practice, an SVD cutoff of 10^{-3} or 10^{-4} is usually a good balance between accuracy and efficiency, and thus, we expect that the DMRG compression error will typically be the main source of error rather than the RK4 error. However, note that even though the DMRG truncation for bond dimension $M = 20$ or SVD cutoff $= 10^{-3}$ leads to a seemingly large wave function error of approximately 10%, the obtained spectrum is still very accurate (see Figure 8), except for some small shifts in the high-frequency region where $\omega/\omega_0 > 2$. This is quite different from the 1-particle and 2-particle approximations, where all the 0−n transitions amplitudes are calculated with large errors except for the 0−0 transition.
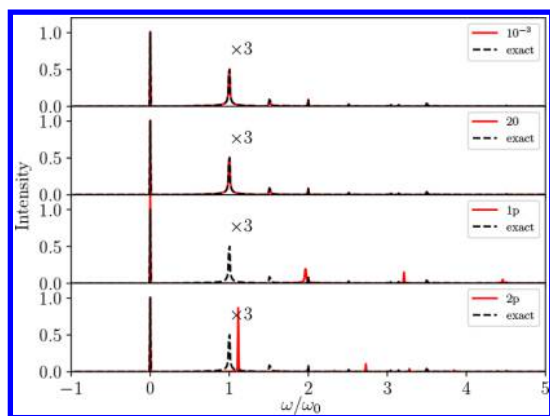
Figure 8. Absorption spectrum at zero temperature calculated by TD-DMRG (SVD cutoff = 10^{-3}), TD-DMRG ($M = 20$), 1-particle approximation and 2-particle approximation. The exact result is also plotted for comparison. (To show the fine structure, the absorption strength is multiplied by 3 when $\omega/\omega_0 > 0.5$.)

3.4. Distyrylbenzene H-Type Aggregates. We conclude our study by considering a TD-DMRG calculation in a realistic H-type aggregate consisting of distyrylbenzenes (DSB).[91] In the DSB crystal, the DSB molecules pack into an intralayer side-by-side herringbone structure shown in Figure 10b. The excitonic coupling between layers can be neglected. Along the direction perpendicular to the layer, the transition dipole moments of the intralayer molecules all align in parallel and form an H-type structure. In addition, there is a small component of the transition dipole moment forming a J-type structure parallel to the layer, resulting in an anisotropic effect of the aggregation on the spectra. We only consider the dominant H-type structure here. We choose a cluster with 18 molecules as our system (see Figure 10b). The parameters of the excitonic coupling and exciton–phonon coupling are adopted from ref 90 (see SI section 4). The linear spectrum of the system has been investigated at a qualitative level using n-particle approximation methods within the Holstein exciton model, and the general features of the spectra have been obtained; however, the fine structure has not been reproduced because only a few (<5) effective modes have been considered.[15,25,92,93] For our TD-DMRG calculations, we chose 14 normal modes for each molecule with a Huang–Rhys factor greater than 0.02. To our knowledge, this is the largest DSB molecular aggregate so far studied for which the fluorescence spectrum is calculated nonperturbatively. The corresponding Hilbert space size for the TD-DMRG (as well as various n-particle approximations) is listed in Table 1.

With the techniques described in Section 2.3, the error of TD-DMRG for the zero-temperature emission spectrum only comes from the DMRG calculation of the lowest state in the one-exciton space. The energy error of this single state is plotted as a function of the bond dimension M in Figure 9 (the

Table 1. System Sizes for TD-DMRG and 1-, 2-Particle Approximation Methods

|	N molecules	N modes	N phonons	dimension of Hilbert space
TD-DMRG	18	14	10	18×10^{252}
1-particle	18	5	4	18 432
2-particle	18	2	4	73 728
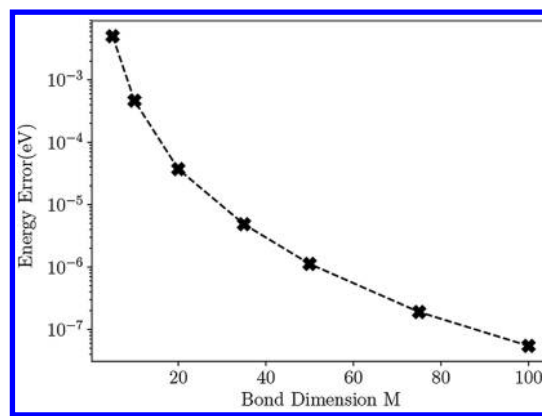
Figure 9. Energy error of the lowest state in the one-exciton space as a function of bond dimension M. (The $M = 500$ energy is taken as the reference.)

energy calculated with $M = 500$ is here regarded as exact). The single-state DMRG calculation in the Holstein model is very accurate, even though the interaction topology in our problem is not one-dimensional. Unlike in purely electronic systems, where $M \sim$ several thousands is often necessary to obtain a converged ground state, in this electron–phonon system, $M = 20$ is already enough to obtain a very accurate result with an error of less than 10^{-4} eV, even though the number of sites is very large (270).

We show the calculated zero-temperature fluorescence spectrum in Figure 10c, and the experimental spectrum at 1.4K is also plotted for comparison.[94] The spectra calculated with $M = 100$ and $M = 20$ are indistinguishable. Thus, not only a single point state but also the spectrum can be accurately obtained with a small M. The TD-DMRG spectrum has three dominant fluorescence bands, 0–1, 0–2, 0–3; the 0–0 band is largely suppressed due to the H-type excitonic coupling. To clearly show the fine structure, the strengths of the 0–2, 0–3 band peaks are multiplied by 2. Compared to the experimental spectrum, most of the fine structure is well reproduced. Nevertheless, the frequency of the vibration which couples most strongly to the exciton in the quantum chemistry derivation of the model is slightly overestimated (1658.65 cm^{-1} from the calculation, ~1435 cm^{-1} from experiment), and the Huang–Rhys factor is underestimated, probably due to the density functional approximation. We also see this discrepancy in the former work, where the spectrum of the DSB dimer is directly treated within the density functional approximation.[95] In the 1-particle approximation calculation, the positions of the main peaks are correct. However, due to the deficiencies we identified in the preceding section, the 0–1 band intensity is severely overestimated, so that the ratio of the 0–2/0–3 band intensities to the 0–1 band intensity is underestimated. Though the 2-particle approximation corrects this problem, the number of vibrational modes which can be included in such calculations is too small to capture the fine structure seen in the TD-DMRG spectrum and in experiment. This demonstrates the superiority of the TD-DMRG methods in systems with large Hilbert spaces which arise when many vibrations need to be considered.

4. CONCLUSIONS

In this work, we implemented the zero-temperature and finite-temperature time-dependent DMRG algorithms (TD-DMRG) for the Holstein Hamiltonian, to calculate the linear absorption
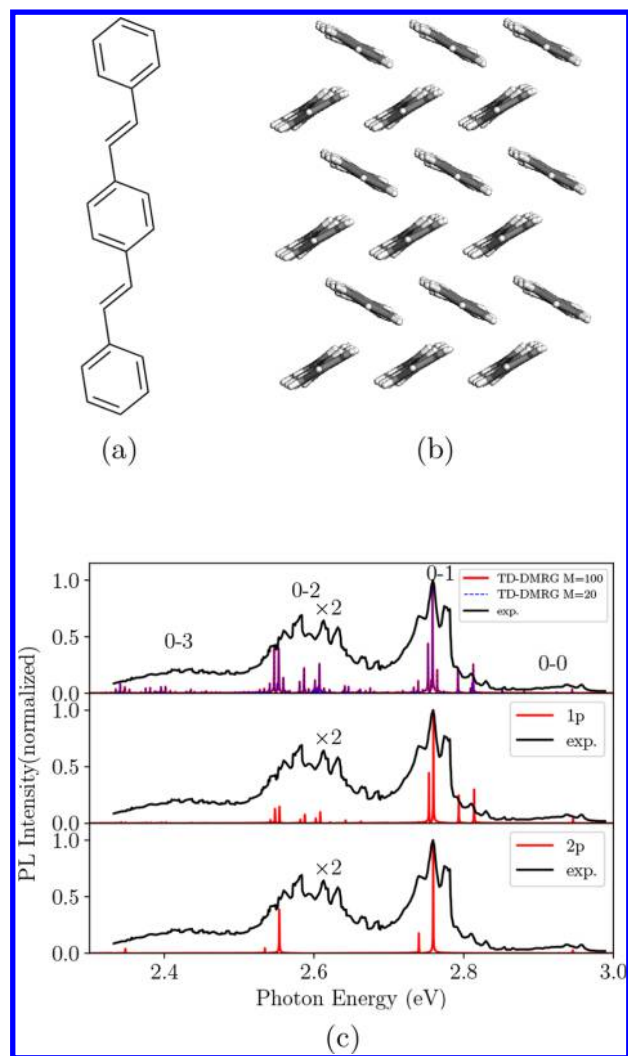
Figure 10. (a) Chemical structure of the DSB molecule. (b) The packing structure of the selected DSB aggregates with 18 molecules. (c) The zero-temperature fluorescence spectrum of DSB aggregates from TD-DMRG (red: $M = 100$, dashed blue: $M = 20$), and the 1-, 2-particle approximations. $\tau = 20$ a.u, $N = 30\,000$, no broadening is applied. The peaks below 2.7 eV are multiplied by 2 to show the fine structure. The experimental results at 1.4K from ref 94 are also plotted (black line).

and fluorescence spectra of molecular aggregates at both zero and finite temperature. Our calculations on PBI molecular chains showed that the practical accuracy of TD-DMRG reaches that of ML-MCTDH at zero temperature and further allows us to extract accurate finite-temperature dynamic properties. The comparison with n-particle approximation methods on both models and the DSB crystal further shows that TD-DMRG is not only much more accurate than these approximations but can also practically handle the larger Hilbert spaces arising from increasing the number of vibrational modes to model detailed spectral features. In summary, our results support the use of TD-DMRG algorithms as accurate, efficient, and robust methods for dynamical problems including both electrons (excitons) and nuclei (phonons). In future work, we will carry out further studies using these TD-DMRG algorithms, including studies of true nonequilibrium phenomena, including charge and energy transport.

■ APPENDIX: MPO FOR THE HOLSTEIN HAMILTONIAN

Multiplying out the matrices in the MPO representation of the Hamiltonian can be thought of as defining a recurrence relation to construct the Hamiltonian with all terms up to site k, from the Hamiltonian and operators up to site $k-1$, and the operators acting on site k.

$$\mathbf{\Omega}_k = \mathbf{\Omega}_{k-1} \cdot \text{MPO}_k \tag{21}$$

$$\mathbf{\Omega}_k = [H_k \quad \mathbf{O}_k \quad 1] \tag{22}$$

Here, $\mathbf{\Omega}_k$ is the MPO obtained by multiplying the local MPO matrices from site 1 to k. H_k represents the part of the Hamiltonian that acts on sites 1 to k, while $\mathbf{O}_k$ represents the row of operators that define an interaction between sites 1 to k and the remaining sites. The general structure of the local MPO matrix of site k is

$$\text{MPO}_k = \begin{bmatrix} 1 & 0 & 0 \\ \mathbf{A}_k & \mathbf{C}_k & 0 \\ B_k & \mathbf{D}_k & 1 \end{bmatrix} \tag{23}$$

$\mathbf{A}_k$ is a column of operators, B_k is a single operator, $\mathbf{C}_k$ is a matrix of operators, and $\mathbf{D}_k$ is a row of operators. The recurrence relation for each component of $\mathbf{\Omega}_k$ is

$$H_k = H_{k-1} \cdot 1 + \mathbf{O}_{k-1} \cdot \mathbf{A}_k + 1 \cdot B_k$$

$$\mathbf{O}_k = \mathbf{O}_{k-1} \cdot \mathbf{C}_k + 1 \cdot \mathbf{D}_k \tag{24}$$

Given the order of sites in the MPS is $e_1, \nu_{11}, ..., \nu_{1n}, ..., e_i, \nu_{i1}, ..., \nu_{in} \cdots$, one of the optimal MPO representation of the Hamiltonian in eq 1 is

(i) For an electronic site before the middle site.

$$\mathbf{A}_k = \begin{bmatrix} J_{0k} a_k \\ J_{0k} a_k^\dagger \\ ... \\ J_{k-1,k} a_k \\ J_{k-1,k} a_k^\dagger \end{bmatrix} \tag{25}$$

$$B_k = [\varepsilon_k a_k^\dagger a_k] \tag{26}$$

$$\mathbf{C}_k = [0 \quad \mathbf{I} \quad 0 \quad 0] \tag{27}$$

$$\mathbf{D}_k = [a_k^\dagger a_k \quad 0 \quad a_k^\dagger \quad a_k] \tag{28}$$

(ii) An electronic site in the middle of the MPS. $\mathbf{A}_k$ and B_k are the same as for case (i)

$$\mathbf{C}_k = \begin{bmatrix} 0 & J_{0,n} & 0 & ... \\ 0 & 0 & J_{0,n} & ... \\ 0 & J_{1,n} & 0 & ... \\ 0 & 0 & J_{1,n} & ... \\ ... & ... & ... & ... \\ 0 & J_{k-1,n} & 0 & ... \\ 0 & 0 & J_{k-1,n} & ... \end{bmatrix} \tag{29}$$

$$\mathbf{D}_k = [a_k^\dagger a_k \quad J_{k,n} a_k^\dagger \quad J_{k,n} a_k \quad ...]$$ (30)

Multiplying out the matrices up to the middle yields a row of operators including complementary operators.

$$\mathbf{\Omega}_k = [H_k \quad a_k^\dagger a_k \quad \mathrm{Com}_n^\dagger \quad \mathrm{Com}_n \quad ... \quad \mathrm{Com}_{k+1}^\dagger \quad \mathrm{Com}_{k+1} \quad 1]$$ (31)

The corresponding complementary operators constructed are

$$\mathrm{Com}_i^\dagger = \sum_{j=1}^{k} J_{i,j} a_j^\dagger$$ (32)

$$\mathrm{Com}_i = \sum_{j=1}^{k} J_{i,j} a_j$$ (33)

(iii) Electronic site after the middle. B_k, $\mathbf{D}_k$ are the same as for case (ii)

$$\mathbf{A}_k = \begin{bmatrix} 0 \\ a_k \\ a_k^\dagger \end{bmatrix}$$ (34)

$$\mathbf{C}_k = [0 \quad \mathbf{I}]$$ (35)

(iv) Vibrational site.

$$\mathbf{A}_k = \begin{bmatrix} g_{in}\omega_{in}(b_{in}^\dagger + b_{in}) \\ 0 \end{bmatrix}$$ (36)

$$B_k = [\omega_{in} b_{in}^\dagger b_{in}]$$ (37)

$$\mathbf{C}_k = [\mathbf{I}]$$ (38)

$$\mathbf{D}_k = [0]$$ (39)

When excitonic coupling terms are 1-dimensional nearest-neighbor, the maximal bond dimension D of MPO constructed above is $\sim$ const, otherwise $D \sim k_e$.

ASSOCIATED CONTENT

S Supporting Information

The Supporting Information is available free of charge on the ACS Publications website at DOI: 10.1021/acs.jctc.8b00628.

Stability analysis of the RK4 method, the comparison of the star/chain representations in TD-DMRG, and the quantum chemistry parameters in the DSB crystal (PDF)

AUTHOR INFORMATION

Corresponding Authors
*E-mail: zgshuai@tsinghua.edu.cn.
*E-mail: gkc1000@gmail.com.
ORCID
Jiajun Ren: 0000-0002-1508-4943
Zhigang Shuai: 0000-0003-3867-2331
Notes
The authors declare no competing financial interest.

REFERENCES

(1) Luo, J.; Xie, Z.; Lam, J. W. Y.; Cheng, L.; Chen, H.; Qiu, C.; Kwok, H. S.; Zhan, X.; Liu, Y.; Zhu, D.; Tang, B. Z. Aggregation-induced emission of 1-methyl-1,2,3,4,5-pentaphenylsilole. *Chem. Commun.* **2001**, 1740–1741.

(2) Engel, G. S.; Calhoun, T. R.; Read, E. L.; Ahn, T.-K.; Mančal, T.; Cheng, Y.-C.; Blankenship, R. E.; Fleming, G. R. Evidence for wavelike energy transfer through quantum coherence in photosynthetic systems. *Nature* **2007**, *446*, 782.

(3) Schröter, M.; Ivanov, S.; Schulze, J.; Polyutov, S.; Yan, Y.; Pullerits, T.; Kühn, O. Exciton–vibrational coupling in the dynamics and spectroscopy of Frenkel excitons in molecular aggregates. *Phys. Rep.* **2015**, *567*, 1–78.

(4) Jang, S.; Newton, M. D.; Silbey, R. J. Multichromophoric Förster resonance energy transfer. *Phys. Rev. Lett.* **2004**, *92*, 218301.

(5) Schröder, M.; Kleinekathöfer, U.; Schreiber, M. Calculation of absorption spectra for light-harvesting systems using non-Markovian approaches as well as modified Redfield theory. *J. Chem. Phys.* **2006**, *124*, 084903.

(6) Tanimura, Y.; Kubo, R. Time evolution of a quantum system in contact with a nearly Gaussian-Markoffian noise bath. *J. Phys. Soc. Jpn.* **1989**, *58*, 101–114.

(7) Chen, L.; Zheng, R.; Shi, Q.; Yan, Y. Optical line shapes of molecular aggregates: Hierarchical equations of motion method. *J. Chem. Phys.* **2009**, *131*, 094502.

(8) Diósi, L.; Strunz, W. T. The non-Markovian stochastic Schrödinger equation for open systems. *Phys. Lett. A* **1997**, *235*, 569–573.

(9) Roden, J.; Strunz, W. T.; Eisfeld, A. Non-Markovian quantum state diffusion for absorption spectra of molecular aggregates. *J. Chem. Phys.* **2011**, *134*, 034902.

(10) Ke, Y.; Zhao, Y. Hierarchy of stochastic Schrödinger equation towards the calculation of absorption and circular dichroism spectra. *J. Chem. Phys.* **2017**, *146*, 174105.

(11) Ke, Y.; Zhao, Y. An extension of stochastic hierarchy equations of motion for the equilibrium correlation functions. *J. Chem. Phys.* **2017**, *146*, 214105.

(12) Makri, N.; Makarov, D. E. Tensor propagator for iterative quantum time evolution of reduced density matrices. I. Theory. *J. Chem. Phys.* **1995**, *102*, 4600–4610.

(13) Philpott, M. Vibronic Coupling in the Exciton States of the Rigid-Lattice Model of Molecular Crystals. *J. Chem. Phys.* **1967**, *47*, 4437–4445.

(14) Hoffmann, M.; Soos, Z. Optical absorption spectra of the Holstein molecular crystal for weak and intermediate electronic coupling. *Phys. Rev. B: Condens. Matter Mater. Phys.* **2002**, *66*, 024305.

(15) Zhao, Z.; Spano, F. C. Vibronic fine structure in the absorption spectrum of oligothiophene thin films. *J. Chem. Phys.* **2005**, *122*, 114701–114701.

(16) Gao, F.; Zhao, Y.; Liang, W. Vibronic spectra of perylene bisimide oligomers: Effects of intermolecular charge-transfer excitation and conformational flexibility. *J. Phys. Chem. B* **2011**, *115*, 2699–2708.

(17) Meyer, H.-D.; Gatti, F.; Worth, G. A. *Multidimensional Quantum Dynamics*; John Wiley & Sons, 2009.

(18) Gagliano, E.; Balseiro, C. Dynamical properties of quantum many-body systems at zero temperature. *Phys. Rev. Lett.* **1987**, *59*, 2999.

(19) Kokalj, J.; Prelovšek, P. Finite-temperature dynamics with the density-matrix renormalization group method. *Phys. Rev. B: Condens. Matter Mater. Phys.* **2009**, *80*, 205117.

(20) Prelovšek, P.; Bonča, J. *Strongly Correlated Systems*; Springer, 2013; pp 1−30.

(21) Szabo, A.; Ostlund, N. S. *Modern Quantum Chemistry: Introduction to Advanced Electronic Structure Theory*; Dover Books, 1996.

(22) Zgid, D.; Gull, E.; Chan, G. K.-L. Truncated configuration interaction expansions as solvers for correlated quantum impurity models and dynamical mean-field theory. *Phys. Rev. B: Condens. Matter Mater. Phys.* **2012**, *86*, 165128.

(23) Spano, F. C. The spectral signatures of Frenkel polarons in H- and J-aggregates. *Acc. Chem. Res.* **2010**, *43*, 429−439.

(24) Song, K.; Bai, S.; Shi, Q. A time domain two-particle approximation to calculate the absorption and circular dichroism line shapes of molecular aggregates. *J. Chem. Phys.* **2015**, *143*, 064109.

(25) Spano, F. C. Excitons in conjugated oligomer aggregates, films, and crystals. *Annu. Rev. Phys. Chem.* **2006**, *57*, 217−243.

(26) Wang, H.; Thoss, M. Multilayer formulation of the multi-configuration time-dependent Hartree theory. *J. Chem. Phys.* **2003**, *119*, 1289−1299.

(27) Worth, G.; Meyer, H.-D.; Köppel, H.; Cederbaum, L.; Burghardt, I. Using the MCTDH wavepacket propagation method to describe multimode non-adiabatic dynamics. *Int. Rev. Phys. Chem.* **2008**, *27*, 569−606.

(28) Matzkies, F.; Manthe, U. Accurate reaction rate calculations including internal and rotational motion: A statistical multi-configurational time-dependent Hartree approach. *J. Chem. Phys.* **1999**, *110*, 88−96.

(29) Manthe, U.; Huarte-Larrañaga, F. Partition functions for reaction rate calculations: statistical sampling and MCTDH propagation. *Chem. Phys. Lett.* **2001**, *349*, 321−328.

(30) Raab, A.; Burghardt, I.; Meyer, H.-D. The multiconfiguration time-dependent Hartree method generalized to the propagation of density operators. *J. Chem. Phys.* **1999**, *111*, 8759−8772.

(31) Raab, A.; Meyer, H.-D. A numerical study on the performance of the multiconfiguration time-dependent Hartree method for density operators. *J. Chem. Phys.* **2000**, *112*, 10718−10729.

(32) McLachlan, A. A variational solution of the time-dependent Schrodinger equation. *Mol. Phys.* **1964**, *8*, 39−44.

(33) White, S. R. Density matrix formulation for quantum renormalization groups. *Phys. Rev. Lett.* **1992**, *69*, 2863.

(34) White, S. R. Density-matrix algorithms for quantum renormalization groups. *Phys. Rev. B: Condens. Matter Mater. Phys.* **1993**, *48*, 10345.

(35) Hallberg, K. A. Density-matrix algorithm for the calculation of dynamical properties of low-dimensional systems. *Phys. Rev. B: Condens. Matter Mater. Phys.* **1995**, *52*, R9827.

(36) Shuai, Z.; Brédas, J.; Saxena, A.; Bishop, A. Linear and nonlinear optical response of polyenes: A density matrix renormalization group study. *J. Chem. Phys.* **1998**, *109*, 2549−2555.

(37) Jeckelmann, E. Dynamical density-matrix renormalization-group method. *Phys. Rev. B: Condens. Matter Mater. Phys.* **2002**, *66*, 045114.

(38) Nishino, T. Density matrix renormalization group method for 2D classical models. *J. Phys. Soc. Jpn.* **1995**, *64*, 3598−3601.

(39) Bursill, R.; Xiang, T.; Gehring, G. The density matrix renormalization group for a quantum spin chain at non-zero temperature. *J. Phys.: Condens. Matter* **1996**, *8*, L583.

(40) Naef, F.; Wang, X.; Zotos, X.; Von der Linden, W. Autocorrelations from the transfer-matrix density-matrix renormalization-group method. *Phys. Rev. B: Condens. Matter Mater. Phys.* **1999**, *60*, 359.

(41) Cazalilla, M.; Marston, J. Time-dependent density-matrix renormalization group: A systematic method for the study of quantum many-body out-of-equilibrium systems. *Phys. Rev. Lett.* **2002**, *88*, 256403.

(42) Luo, H.; Xiang, T.; Wang, X. Comment on Time-dependent density-matrix renormalization group: a systematic method for the study of quantum many-body out-of-equilibrium systems. *Phys. Rev. Lett.* **2003**, *91*, 049701.

(43) Vidal, G. Efficient simulation of one-dimensional quantum many-body systems. *Phys. Rev. Lett.* **2004**, *93*, 040502.

(44) White, S. R.; Feiguin, A. E. Real-time evolution using the density matrix renormalization group. *Phys. Rev. Lett.* **2004**, *93*, 076401.

(45) Daley, A. J.; Kollath, C.; Schollwöck, U.; Vidal, G. Time-dependent density-matrix renormalization-group using adaptive effective Hilbert spaces. *J. Stat. Mech.: Theory Exp.* **2004**, *2004*, P04005.

(46) Feiguin, A. E.; White, S. R. Time-step targeting methods for real-time dynamics using the density matrix renormalization group. *Phys. Rev. B: Condens. Matter Mater. Phys.* **2005**, *72*, 020404.

(47) M, K. J.; C, R. C.; Garnet, K. C. *Quantum Information and Computation for Chemistry*; Wiley-Blackwell, 2014; pp 179−192.

(48) Haegeman, J.; Cirac, J. I.; Osborne, T. J.; Pižorn, I.; Verschelde, H.; Verstraete, F. Time-dependent variational principle for quantum lattices. *Phys. Rev. Lett.* **2011**, *107*, 070601.

(49) Haegeman, J.; Lubich, C.; Oseledets, I.; Vandereycken, B.; Verstraete, F. Unifying time evolution and optimization with matrix product states. *Phys. Rev. B: Condens. Matter Mater. Phys.* **2016**, *94*, 165116.

(50) Dorando, J. J.; Hachmann, J.; Chan, G. K.-L. Analytic response theory for the density matrix renormalization group. *J. Chem. Phys.* **2009**, *130*, 184111.

(51) Verstraete, F.; Garcia-Ripoll, J. J.; Cirac, J. I. Matrix product density operators: simulation of finite-temperature and dissipative systems. *Phys. Rev. Lett.* **2004**, *93*, 207204.

(52) Zwolak, M.; Vidal, G. Mixed-state dynamics in one-dimensional quantum lattice systems: a time-dependent superoperator renormalization algorithm. *Phys. Rev. Lett.* **2004**, *93*, 207205.

(53) Feiguin, A. E.; White, S. R. Finite-temperature density matrix renormalization using an enlarged Hilbert space. *Phys. Rev. B: Condens. Matter Mater. Phys.* **2005**, *72*, 220401.

(54) Barthel, T. Precise evaluation of thermal response functions by optimized density matrix renormalization group schemes. *New J. Phys.* **2013**, *15*, 073010.

(55) Shuai, Z.; Bredas, J.; Pati, S.; Ramasesha, S. Quantum confinement effects on the ordering of the lowest-lying excited states in conjugated polymers. *Proceedings of the SPIE - The International Society for Optical Engineering* **1997**, *3145*, 283−302.

(56) Chan, G. K.-L.; Sharma, S. The density matrix renormalization group in quantum chemistry. *Annu. Rev. Phys. Chem.* **2011**, *62*, 465−481.

(57) Ronca, E.; Li, Z.; Jimenez-Hoyos, C. A.; Chan, G. K.-L. Time-step targeting time-dependent and dynamical density matrix renormalization group algorithms with ab initio Hamiltonians. *J. Chem. Theory Comput.* **2017**, *13*, 5560−5571.

(58) Caron, L.; Moukouri, S. Density matrix renormalization group applied to the ground state of the XY spin-Peierls system. *Phys. Rev. Lett.* **1996**, *76*, 4050.

(59) Jeckelmann, E.; White, S. R. Density-matrix renormalization-group study of the polaron problem in the Holstein model. *Phys. Rev. B: Condens. Matter Mater. Phys.* **1998**, *57*, 6376.

(60) Tozer, O. R.; Barford, W. Localization of large polarons in the disordered Holstein model. *Phys. Rev. B: Condens. Matter Mater. Phys.* **2014**, *89*, 155434.

(61) Barford, W.; Marcus, M.; Tozer, O. R. Polarons in π-conjugated polymers: Anderson or Landau? *J. Phys. Chem. A* **2016**, *120*, 615−620.

(62) García, D. J.; Hallberg, K.; Rozenberg, M. J. Dynamical mean field theory with the density matrix renormalization group. *Phys. Rev. Lett.* **2004**, *93*, 246403.

(63) Ganahl, M.; Aichhorn, M.; Evertz, H. G.; Thunström, P.; Held, K.; Verstraete, F. Efficient DMFT impurity solver using real-time dynamics with matrix product states. *Phys. Rev. B: Condens. Matter Mater. Phys.* **2015**, *92*, 155132.

(64) Wolf, F. A.; McCulloch, I. P.; Schollwöck, U. Solving oonequilibrium dynamical mean-field theory using matrix product states. *Phys. Rev. B: Condens. Matter Mater. Phys.* **2014**, *90*, 235131.

(65) Hallberg, K.; García, D.; Cornaglia, P. S.; Facio, J. I.; Núñez-Fernández, Y. State-of-the-art techniques for calculating spectral functions in models for correlated materials. *Europhys. Lett.* **2015**, *112*, 17001.

(66) Prior, J.; Chin, A. W.; Huelga, S. F.; Plenio, M. B. Efficient simulation of strong system-environment interactions. *Phys. Rev. Lett.* **2010**, *105*, 050404.

(67) Chin, A.; Prior, J.; Rosenbach, R.; Caycedo-Soler, F.; Huelga, S.; Plenio, M. The role of non-equilibrium vibrational structures in electronic coherence and recoherence in pigment−protein complexes. *Nat. Phys.* **2013**, *9*, 113.

(68) Yao, Y.; Duan, L.; Lü, Z.; Wu, C.-Q.; Zhao, Y. Dynamics of the sub-Ohmic spin-boson model: A comparison of three numerical approaches. *Phys. Rev. E* **2013**, *88*, 023303.

(69) Yao, Y.; Xie, X.; Ma, H. Ultrafast Long-Range Charge Separation in Organic Photovoltaics: Promotion by Off-Diagonal Vibronic Couplings and Entropy Increase. *J. Phys. Chem. Lett.* **2016**, *7*, 4830−4835.

(70) Yao, Y.; Sun, K.-W.; Luo, Z.; Ma, H. Full Quantum Dynamics Simulation of a Realistic Molecular System Using the Adaptive Time-Dependent Density Matrix Renormalization Group Method. *J. Phys. Chem. Lett.* **2018**, *9*, 413−419.

(71) Merrifield, R. Ionized States in a One-Dimensional Molecular Crystal. *J. Chem. Phys.* **1961**, *34*, 1835−1839.

(72) Hoffmann, M. Mixing of Frenkel and charge-transfer excitons and their quantum confinement in thin films. *Thin Films Nanostruct.* **2003**, *31*, 221−292.

(73) Chorošajev, V.; Marčiulionis, T.; Abramavicius, D. Temporal dynamics of excitonic states with nonlinear electron-vibrational coupling. *J. Chem. Phys.* **2017**, *147*, 074114.

(74) de Vega, I.; Schollwöck, U.; Wolf, F. A. How to discretize a quantum bath for real-time evolution. *Phys. Rev. B: Condens. Matter Mater. Phys.* **2015**, *92*, 155126.

(75) Chin, A. W.; Rivas, Á.; Huelga, S. F.; Plenio, M. B. Exact mapping between system-reservoir quantum models and semi-infinite discrete chains using orthogonal polynomials. *J. Math. Phys.* **2010**, *51*, 092109.

(76) Shenvi, N.; Schmidt, J.; Edwards, S. T.; Tully, J. C. Efficient discretization of the continuum through complex contour deformation. *Phys. Rev. A: At., Mol., Opt. Phys.* **2008**, *78*, 022502.

(77) Metzner, W.; Vollhardt, D. Correlated lattice fermions in d= dimensions. *Phys. Rev. Lett.* **1989**, *62*, 324.

(78) Schollwöck, U. The density-matrix renormalization group in the age of matrix product states. *Ann. Phys.* **2011**, *326*, 96−192.

(79) Shi, Y.-Y.; Duan, L.-M.; Vidal, G. Classical simulation of quantum many-body systems with a tree tensor network. *Phys. Rev. A: At., Mol., Opt. Phys.* **2006**, *74*, 022320.

(80) Nakatani, N.; Chan, G. K.-L. Efficient tree tensor network states (TTNS) for quantum chemistry: Generalizations of the density matrix renormalization group algorithm. *J. Chem. Phys.* **2013**, *138*, 134113.

(81) Chan, G. K.-L.; Keselman, A.; Nakatani, N.; Li, Z.; White, S. R. Matrix product operators, matrix product states, and ab initio density matrix renormalization group algorithms. *J. Chem. Phys.* **2016**, *145*, 014102.

(82) Zaletel, M. P.; Mong, R. S.; Karrasch, C.; Moore, J. E.; Pollmann, F. Time-evolving a matrix product state with long-ranged interactions. *Phys. Rev. B: Condens. Matter Mater. Phys.* **2015**, *91*, 165112.

(83) Takahasi, Y.; Umezawa, H. *Collective Phenomena*; Gordon and Breach, Science Publishers: London, 1975; Vol. 2, pp 55−80.

(84) Borrelli, R.; Gelin, M. F. Quantum electron-vibrational dynamics at finite temperature: Thermo field dynamics approach. *J. Chem. Phys.* **2016**, *145*, 224101.

(85) Karrasch, C.; Bardarson, J.; Moore, J. Finite-temperature dynamical density matrix renormalization group and the drude weight of spin-1/2 chains. *Phys. Rev. Lett.* **2012**, *108*, 227206.

(86) Kasha, M. Energy transfer mechanisms and the molecular exciton model for molecular aggregates. *Radiat. Res.* **1963**, *20*, 55−70.

(87) Würthner, F. Perylene bisimide dyes as versatile building blocks for functional supramolecular architectures. *Chem. Commun.* **2004**, 1564−1579.

(88) Ambrosek, D.; Kohn, A.; Schulze, J.; Kuhn, O. Quantum chemical parametrization and spectroscopic characterization of the frenkel exciton hamiltonian for a J-aggregate forming perylene bisimide dye. *J. Phys. Chem. A* **2012**, *116*, 11451−11458.

(89) Li, X.-Q.; Zhang, X.; Ghosh, S.; Würthner, F. Highly Fluorescent Lyotropic Mesophases and Organogels Based on J-Aggregates of Core-Twisted Perylene Bisimide Dyes. *Chem. - Eur. J.* **2008**, *14*, 8074−8078.

(90) Li, W; Peng, Q.; Xie, Y.; Zhang, T.; Shuai, Z. Effect of intermolecular excited-state interaction on vibrationally resolved optical spectra in organic molecular aggregates. *Huaxue Xuebao* **2016**, *74*, 902−909.

(91) Wu, C.; Delong, M.; Vardeny, Z.; Ferraris, J. Structual and optical studies of distyrylbenzene single crystals. *Synth. Met.* **2003**, *137*, 939−941.

(92) Spano, F. C. Absorption and emission in pinwheel aggregates of oligo-phenylene vinylene molecules. *J. Chem. Phys.* **2001**, *114*, 5376−5390.

(93) Spano, F. C. The fundamental photophysics of conjugated oligomer herringbone aggregates. *J. Chem. Phys.* **2003**, *118*, 981−994.

(94) Wu, C.; Korovyanko, O.; Delong, M.; Vardeny, Z.; Ferraris, J. Optical studies of distyrylbenzene single crystals. *Synth. Met.* **2003**, *139*, 735−738.

(95) Wykes, M.; Parambil, R.; Beljonne, D.; Gierschner, J. Vibronic coupling in molecular crystals: A Franck-Condon Herzberg-Teller model of H-aggregate fluorescence based on quantum chemical cluster calculations. *J. Chem. Phys.* **2015**, *143*, 114116.